

Probing the Merger Rates of Supermassive Black Holes and Galaxies with Gravitational Waves

Yun Fang ^{1,2}★ Rong-Gen Cai,^{1,2}†

¹*Institute of Fundamental Physics and Quantum Technology, Ningbo University, Ningbo, 315211, China*

²*School of Physical Science and Technology, Ningbo University, Ningbo, 315211, China*

Accepted XXX. Received YYY; in original form ZZZ

ABSTRACT

The mergers of galaxies and supermassive black holes (SMBHs) are key drivers of galaxy evolution, contributing to the growth of both galaxies and their central black holes. Current and upcoming gravitational wave (GW) detectors—Pulsar Timing Arrays (PTAs), LISA, Taiji, and Tianqin—offer unique access to these processes by observing GW signals from SMBH binaries. We present a framework to infer galaxy and SMBH merger rates by combining mock LISA detections of SMBH mergers with PTA constraints on the stochastic GW background, while incorporating observational uncertainties in stellar mass functions and M_{\bullet} – M_* relations. We find that the number of LISA-detected events and their joint distribution in mass and redshift are key to constraining merger rates—datasets with around forty events yield results consistent with galaxy pair observations, whereas limited event counts lead to biases at high redshift. Including PTA data further reduces parameter uncertainties. Our method also effectively constrains the delay time between galaxy and SMBH mergers, with longer delays suppressing high-redshift SMBH merger rates and shifting mass growth from mergers to accretion. According to our mock analysis, the models with delay times longer than 0.5Gyr (0.8Gyr), accretion becomes the primary driver of SMBH mass growth beyond $z \sim 6$ (4). In contrast, the SMBH occupation fraction at $z > 3$ remains poorly constrained due to its degeneracies with delay time and the galaxy merger rate. These findings highlight both the promise and limitations of using GW observations to probe the coevolution of galaxies and SMBHs.

Key words: gravitational waves – supermassive black holes – galaxies – merger rate – methods: Bayesian inference

1 INTRODUCTION

Supermassive black holes (SMBHs) are ubiquitous in the centers of massive galaxies. Observations reveal that SMBHs are intimately linked to the properties of their host galaxies, as demonstrated by scaling relationships like the M_{\bullet} – σ and M_{\bullet} – M_* relations (Ferrarese & Merritt 2000; Gebhardt et al. 2000; Kormendy & Ho 2013), which link the mass of the SMBH M_{\bullet} to the velocity dispersion σ of the galaxy bulge and the galaxy stellar mass (M_*). This intimate relationship suggests a co-evolution of SMBHs and their host galaxies throughout the universe.

Galaxies are hierarchically assembled through the mergers of dark matter halos. When two galaxies merge, their central SMBHs form pairs at large separations. Over time, these black holes lose energy via dynamical friction, interactions with gas and stars, and eventually settle into a regime where gravitational radiation dominates (Begelman et al. 1980; Yu 2002; Escala et al. 2005). Ultimately, they coalesce into a single, more massive black hole. Throughout galaxy evolution, SMBHs assemble their mass through both gas accretion and hierarchical mergers, with accretion generally considered as the dominant process and merger becomes significant for massive SMBHs at low

redshifts (e.g. Soltan 1982; Marconi et al. 2004; Hopkins et al. 2006; Volonteri 2012; Pacucci & Loeb 2020). Understanding the evolutionary history of SMBHs and their coevolution with host galaxies is vital for unraveling the processes driving galaxy formation and evolution, as well as the emergence of the large-scale structure of the universe.

One of the recent spotlight observations comes from the pulsar timing arrays (PTAs): the North American Nanohertz Observatory for Gravitational Waves (NANOGrav) (Agazie et al. 2023), the European PTA (EPTA) in conjunction with the Indian PTA (InPTA) (Antoniadis et al. 2023a,b), the Parkes PTA (PPTA) (Reardon et al. 2023), and the Chinese PTA (CPTA) (Xu et al. 2023) announced the evidence for a signal consistent with a stochastic gravitational wave background (SGWB). This SGWB signal is most likely generated by SMBH binaries across the universe during their inspiraling phase at sub-parsec separations. The strain amplitude of the SGWB constrained by PTAs, assuming quasi-circular orbits for SMBH binaries, suggests that SMBH binaries experience no delay or short delay timescale between the merger of SMBHs and galaxies (Antoniadis et al. 2024). This finding implies that the "final parsec problem" (Milosavljević & Merritt 2001; Yu 2002; Milosavljević & Merritt 2003) may not be a significant barrier. A short delay timescale could be explained if the SMBH binaries reside in a triaxial stellar distribution (e.g. Yu 2002; Merritt & Poon 2004; Holley-Bockelmann

★ E-mail: fangyun@nbu.edu.cn

† E-mail: caironggen@nbu.edu.cn

& Sigurdsson 2006; Gualandris et al. 2016), a gas-rich environment (e.g. Armitage & Natarajan 2002; Dotti et al. 2006; Haiman et al. 2009), or if the SMBHs have undergone multiple mergers (Hoffman & Loeb 2007).

Another major highlight comes from recent discoveries by the James Webb Space Telescope (JWST) (Übler et al. 2023; Larson et al. 2023; Harikane et al. 2023; Bogdan et al. 2024; Ding et al. 2023; Maiolino et al. 2023; Yue et al. 2024; Kocevski et al. 2023; Stone et al. 2024) and the observations of scaling relationships at redshifts $z > 4$ from a population of SMBHs (Pacucci et al. 2023; Li et al. 2024; Matthee et al. 2024). Notably, JWST observations suggest that the masses of SMBHs at $4 < z < 7$ are one to two orders of magnitude larger than those predicted by the local $M_{\bullet} - M_{*}$ relation (Pacucci et al. 2023), albeit with a larger scatter. The theoretical model has been proposed to explain these JWST findings (Pacucci & Loeb 2024). However, there is also speculation that this apparent offset toward higher SMBH masses may be due to observational biases (Li et al. 2024).

Future projects such as the Laser Interferometer Space Antenna (LISA) (Seoane et al. 2013; Amaro-Seoane et al. 2017a), Taiji (Hu & Wu 2017; Ruan et al. 2018), and Tianqin (Luo et al. 2016) are designed to detect millihertz gravitational waves (GWs) generated by SMBH binary mergers. While both PTAs and LISA-like detectors are able to detect GWs from SMBH binaries, they are complementary in their capabilities. PTAs are designed to measure GWs from individual SMBH binaries and/or the SGWB produced by unresolved SMBH binaries, primarily within the mass range of $10^8 - 10^9 M_{\odot}$. In contrast, LISA-like detectors are optimized to detect GWs from merging SMBH binaries with masses in the range of $10^3 - 10^8 M_{\odot}$. Given that gravitational radiation from SMBH binary mergers represents some of the most energetic events in the universe, the signals are expected to be so strong that LISA will be able to detect them with high signal to noise ratio, potentially enabling the detection of such sources out to redshifts as high as $z \sim 20 - 30$ (Amaro-Seoane et al. 2017a). By comparison, for PTAs, the SGWB is dominated by SMBH binaries within $z \sim 3$ (e.g. Sesana 2013b), and the detection of individual binaries is typically limited to redshifts of $z \sim 1$ (e.g. Sesana et al. 2009).

Detecting GWs from SMBH binaries is crucial for revealing the formation and evolutionary histories of SMBHs. Such observations enable the estimation of their merger rates (e.g. Klein et al. 2016; Katz et al. 2019; Antoniadis et al. 2024; Bi et al. 2023), the differentiation between seeding models (Klein et al. 2016), the investigation of their evolutionary timescales (e.g. Fang & Yang 2023; Chen et al. 2023; Antoniadis et al. 2024), and determining the role mergers play in SMBH mass assemble (e.g. Pacucci & Loeb 2020; Valiante et al. 2021) as well as in shaping scaling relationships (e.g. Volonteri & Natarajan 2009; Shankar et al. 2016; Simon & Burke-Spolaor 2016).

In this work, we estimate the merger rate of SMBHs and galaxies from GW detection with mock LISA GW data and the current PTA detection of SGWB strain (e.g. Agazie et al. 2023). Since direct observations of SMBH pairs, binaries, and their mergers are challenging, SMBH merger rates are typically inferred indirectly from galaxy merger rates, e.g., using the scaling relationships between SMBHs and their host galaxies. We adopt the local $M_{\bullet} - M_{*}$ scaling relationship from Kormendy & Ho (2013) for $z < 4$ and incorporate JWST results (Pacucci & Loeb 2024) for $z > 4$. The galaxy merger rate is determined as the product of the galaxy merger rate per galaxy and the galaxy stellar mass function (GSMF). The GSMF is well-constrained at low and intermediate redshifts, and we utilize its observational results extending up to $z \sim 10$ (Baldry et al. 2012; Huertas-Company et al. 2016; Santini et al. 2012; McLeod et al. 2021; Song et al.

2016; Stefanon et al. 2021). The galaxy merger rate per galaxy however remains uncertain. It is either inferred from electromagnetic observations of galaxy pairs—calculated as the galaxy pair fraction divided by an assumed delay time between pair formation and merger (e.g. Sesana 2013a; Duncan et al. 2019a; Duan et al. 2024)—or predicted through theoretical models (e.g. Rodriguez-Gomez et al. 2015; O’Leary et al. 2021). We parameterize the galaxy merger rate per galaxy with hyper-parameters, which, together with the delay time of SMBH mergers and the SMBH occupation fraction, constitute the model parameters. In the process of estimation of model parameters, mock LISA GW data for representative examples are generated, while accounting for model uncertainties from observational uncertainties in both the GSMFs and the $M_{\bullet} - M_{*}$ relationship at different redshift bins. Our discussion focuses on following aspects: 1. The capability of the method developed here to constrain the galaxy merger rate per galaxy, the delay time of SMBH mergers, and the SMBH occupation fraction for low-mass galaxies; 2. A comparison between the galaxy merger rates inferred from GW detections and those derived from galaxy pair observations and cosmological simulations; 3. An analysis of SMBH mass assembly, comparing the contributions from mergers and accretion, as well as the influence of the delay timescale on the SMBH merger rate and mass assembly.

This paper is organized as follows. In Section 2, we outline the framework for constructing the merger rate of SMBH binaries. Section 3 presents the derivation of the SGWB strain from a population of SMBH binaries. In Section 4, we introduce the population analysis framework for LISA GW data. Section 5 is devoted to inferring galaxy and SMBH merger rates from mock LISA data, in combination with PTA constraints. Specifically, we estimate model parameters under two merger rate models in subsections 5.1.1–5.1.3, compare galaxy merger rates inferred from GW detection with those from observations of galaxy pairs and simulations in subsection 5.1.4, estimate the delay time of SMBH binary coalescence in subsection 5.2, discuss SMBH mass assembly contributed by mergers and accretion in subsection 5.3, and analyze the SMBH occupation fraction in subsection 5.4. Finally, we conclude our work in Section 6.

In the context, we adopt a Λ CDM cosmology with $H_0 = 70 \text{ km s}^{-1} \text{ Mpc}^{-1}$, $\Omega_M = 0.3$, and $\Omega_{\Lambda} = 0.7$ at $z = 0$.

2 THE MERGER RATE OF SMBH BINARIES

Galaxy mergers bring together their SMBHs, forming SMBH pairs. During major mergers, dynamical friction works as a main process that drives the SMBHs toward the center of the common nucleus of the newly formed galaxy, where they eventually form a Keplerian binary at separations of a few parsecs (Begelman et al. 1980; Yu 2002; Mayer et al. 2007; Callegari et al. 2009; Chapon et al. 2013; Pfister et al. 2017; Sayeb et al. 2021). The subsequent evolution of the binary orbit depends on interactions with the surrounding environment. Over a characteristic dynamical timescale, the SMBH binary sinks to sub-parsec separations, where gravitational radiation becomes the dominant mechanism driving orbital decay. At this stage, the binary emits GWs in the nanohertz frequency band, contributing to the SGWB detectable by PTAs. Finally, the SMBH binary coalesces due to energy dissipation via gravitational radiation, producing GW signals that could be detected by detectors like LISA.

The merger rate of SMBH binaries, $\frac{d^3n}{dz dM_{\bullet} dq_{\bullet}}$, is determined by the SMBH mass function, $\Phi_{\bullet}(z, M_{\bullet})$, and the merger rate per

SMBH, $\mathcal{R}_\bullet(z, M_\bullet, q_\bullet)$,

$$\frac{d^3 n_\bullet}{dz dM_\bullet dq_\bullet} = \Phi_\bullet(z, M_\bullet) \mathcal{R}_\bullet(z, M_\bullet, q_\bullet), \quad (1)$$

where q_\bullet is the mass ratio of the merging SMBHs.

A scaling relation is commonly employed to connect the merger rate of SMBH binaries to the merger rate of galaxies, to be specific,

$$\begin{aligned} \frac{d^3 n_\bullet}{dz dM_\bullet dq_\bullet} &= |\Phi_{\text{Gal}} \mathcal{R}_{\text{Gal}}|_{\text{Gal} \rightarrow \bullet} \\ &= f_{\text{occ}} \frac{d^3 n_{\text{Gal}}}{dz dX_{\text{Gal}} dq_{\text{Gal}}} \frac{dX_{\text{Gal}}}{dM_\bullet} \frac{dq_{\text{Gal}}}{dq_\bullet}, \quad (2) \end{aligned}$$

where X_{Gal} denotes the property of host galaxy, such as the stellar mass M_* , the budge mass M_{budge} , or the velocity dispersion σ , q_{Gal} is the mass ratio of the host galaxies, and f_{occ} is the SMBH occupation fraction of galaxy.

It has been suggested (Pacucci et al. 2023; Maiolino et al. 2023) that the $M_\bullet - \sigma$ relation is more fundamental, as it exhibits smaller scatter and remains largely invariant across redshifts compared to the $M_\bullet - M_*$ relation, which is subject to greater uncertainty, and hints of evolution with redshift. However, the galaxy velocity dispersion function, $\Phi_{\text{Gal}}(\sigma)$, is poorly constrained, particularly at high redshifts (Taylor et al. 2022; Matt et al. 2023). In contrast, the GSMF has been properly measured up to $z \sim 10$ (Baldry et al. 2012; Huertas-Company et al. 2016; Santini et al. 2012; McLeod et al. 2021; Song et al. 2016; Stefanon et al. 2021). Since in this work, we consider the detection with LISA which is supposed to measure GW events at high redshift, the $M_\bullet - M_*$ relation is adopted here. Consequently, X_{Gal} in equation (2) represents M_* .

The $M_\bullet - M_*$ relationship could be parameterized as,

$$\log_{10} \left(\frac{M_\bullet}{M_\odot} \right) = \mathcal{N} \left(a + b \log_{10} \left(\frac{M_*}{M_\odot} \right), \epsilon \right), \quad (3)$$

where $\mathcal{N}(\mu, \epsilon)$ represents a normal distribution with a mean value of μ and a scatter of ϵ . We now denote the parameters $\{a, b, \epsilon\}$ as $\Lambda_{M_\bullet - M_*}$ in the following context.

The scatter in the $M_\bullet - M_*$ relationship has a significant impact on the derived mass function and the merger rate of SMBHs (e.g. Simon & Burke-Spolaor 2016; Simon 2023). Additionally, there is typically a delay time τ between the merger of the SMBH binary and the merger of their host galaxies. To account for the delay time and the uncertainties arising from the scaling relationship, the merger rate of SMBH binaries is expressed as (e.g., Fang & Yang 2023),

$$\begin{aligned} \frac{d^2 n_\bullet}{dz dM_\bullet} (z, M_* | \Lambda) &= \\ \frac{dt_L}{dz} \int \frac{d^2 n_{\text{Gal}}}{dz dM_*} (t_L + \tau, M_* | \Lambda_m) f_{\text{occ}} P_{\text{delay}}(\tau | \Lambda_d) P(M_\bullet | M_*) dM_* d\tau \quad (4) \end{aligned}$$

where t_L is the lookback time, $P(M_\bullet | M_*)$ is the conditional probability determined by equation (3), $P_{\text{delay}}(\tau | \Lambda_d)$ is an arbitrary distribution of delay time parameterized with Λ_d , and the galaxy merger rate $\frac{d^2 n_{\text{Gal}}}{dz dM_*} (t_L + \tau, M_* | \Lambda_{\text{dN/dt}})$ is parameterized with $\Lambda_{\text{dN/dt}}$. The model of SMBH merger rate is then given by model parameters $\Lambda = \{\Lambda_m, \Lambda_d, f_{\text{occ}}\}$. We neglect the time SMBH binaries spend emitting in the nanohertz band prior to merger. This approximation is due to the fact that this time is typically much smaller than the Hubble time.

In this work, we focus on major galaxy mergers, restricting the mass ratio q_{Gal} to the range $[1/4, 1]$. The galaxy merger rate is averaged over mass ratios within this range. Consequently, the galaxy

merger rate is expressed as:

$$\frac{d^2 n_{\text{Gal}}}{dz dM_*} = \Phi_{\text{GSMF}}(M_*, z) \mathcal{R}_{\text{Gal}}(M_*, z), \quad (5)$$

where $\Phi_{\text{GSMF}}(M_*, z)$ is the GSMF which is given by a (double) Schechter function as

$$\begin{aligned} \Phi_{\text{GSMF}} &= \ln 10 \exp \left(-10^{\log_{10}(M_* - M_\star)} \right) \\ &\times \left(\phi_1 10^{(\log_{10}(M_* - M_\star))(a_1+1)} + \phi_2 10^{(\log_{10}(M_* - M_\star))(a_2+1)} \right). \quad (6) \end{aligned}$$

Hereafter, we collectively denote the parameters $\{M_\star, \phi_1, a_1, \phi_2, a_2\}$ in the GSMFs as Λ_{GSMF} .

3 SGWB FROM SMBH BINARY POPULATION

The characteristic strain spectrum, $h_c^2(f)$, from a cosmic population of SMBH binaries emitting GWs within a frequency bin df , as observed on Earth, is given by:

$$h_c^2(f) = f \int \int \int dz dM_\bullet dq_\bullet h_s^2 \frac{d^4 N}{dz dM_\bullet dq_\bullet df}, \quad (7)$$

where $d^4 N$ represents the number of SMBH binaries within a given redshift range dz , primary black hole mass range dM_\bullet , and mass ratio range dq_\bullet , which are emitting GWs within a frequency range df . Additionally, h_s denotes the polarization- and sky-averaged GW strain contributed by each individual source, which writes,

$$h_s = \sqrt{\frac{32}{5}} \left(\frac{GM_c}{c^3} \right)^{5/3} \frac{(\pi f_{\text{r}})^{2/3} c}{D_c}, \quad (8)$$

where $M_c = M_\bullet (q_\bullet^3 / (1 + q_\bullet))^{1/5}$ is the chirp mass of the binary, D_c is the proper (co-moving) distance to the binary, and f_{r} is the frequency of the GWs emitted in the rest frame of the binary. The Earth-observed GW frequency f is related to f_{r} by $f = f_{\text{r}} / (1 + z)$.

We further rewrite the term $\frac{d^4 N}{dz dM_\bullet dq_\bullet df}$ in equation (7) as,

$$\frac{d^4 N}{dz dM_\bullet dq_\bullet df} = \frac{d^3 n_\bullet}{dz dM_\bullet dq_\bullet} \frac{dV}{dz} \frac{dz}{dt} \frac{dt}{df}. \quad (9)$$

The conversion above transforms the number of binaries per co-moving volume element, dV , into the number of binaries per GW frequency bin, df , by first converting to redshift, and then to the Earth-observed time. Once a binary hardens and decouples from its surrounding galactic environment, the evolution of its orbit becomes dominated by the emission of gravitational radiation, occurring at a rate given by:

$$\frac{df_{\text{orb}}}{dt} = \frac{96}{5} \left(\frac{GM_c}{c^3} \right)^{5/3} (2\pi)^{8/3} f_{\text{orb}}^{11/3}, \quad (10)$$

where f_{orb} is the orbital frequency in the rest frame. For binaries in a circular orbit, the frequency of GWs emitted in the rest frame is given by $f_{\text{r}} = 2f_{\text{orb}}$.

The frequency dependence of h_c is encoded in both h_s and dt/df . By combining Eqs. 7-10, $h_c(f)$ can be expressed as a simple power-law with a dimensionless amplitude A_{yr} referenced to a characteristic frequency of $f_{\text{yr}} = 1 \text{ yr}^{-1}$,

$$h_c(f) = A_{\text{yr}} \left(\frac{f}{f_{\text{yr}}} \right)^{-2/3}. \quad (11)$$

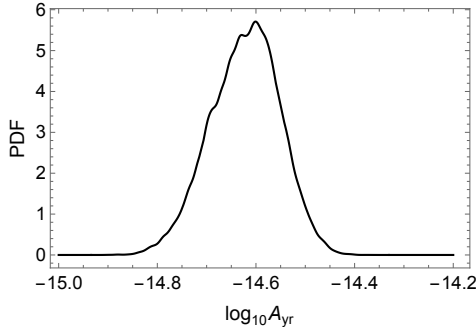


Figure 1. Strain amplitude of SGWB detected by NANOGrav (Agazie et al. 2023).

By substituting equation (2) into equation (9), and then into equation (7), and integrating over the mass ratio for major mergers, the strain of SGWB is finally given by:

$$h_c^2 = f \int \int \int \Phi_{\text{GSMF}}(M_*, z') \frac{dN}{dt}(M_*, z') \frac{dV}{dz} \left(\frac{dt}{df} h_s^2 \right) dz dM_*, \quad (12)$$

where $z' = z(t_L(z) + \tau)$ represents the redshift at which the galaxy merger occurs, while z denotes the redshift at which the SMBH binary emits GWs in the PTA frequency band.

The strain amplitude of SGWB observed by NANOGrav (Agazie et al. 2023) assuming quasi-circular orbit for SMBH binary is shown in Fig. 1. Similar strain amplitudes have been reported by other PTAs (Antoniadis et al. 2023a,b; Reardon et al. 2023; Xu et al. 2023). We use this strain amplitude to constrain the merger rates of SMBHs and their host galaxies in Section 5.

4 DETECTING SMBH BINARY MERGER EVENTS WITH LISA

LISA is expected to detect between a few to several hundred SMBH binary mergers per year (e.g. Sesana et al. 2007; Klein et al. 2016), depending on the redshift and mass range. The detection rate is highly sensitive to the assumptions about galaxy formation, SMBH growth, and the efficiency of binary mergers (e.g. Volonteri et al. 2003; Sesana et al. 2007; Barusse 2012; Klein et al. 2016). In this section, we demonstrate how the merger rate of SMBH binaries can be inferred from LISA GW events. The mass of the merging SMBHs is considered in the range $[10^5 M_\odot, 10^8 M_\odot]$. The lower limit reflects the smallest SMBH masses observed in galactic centers, while the upper limit corresponds to LISA's detection threshold, as determined by its signal-to-noise ratio curve.

4.1 Population Analysis Framework

The hierarchical Bayesian approach is a widely used method for inferring the underlying distribution of a population based on a set of observed events that statistically follow it. This distribution is typically described by a theoretical model parameterized by a few hyperparameters. The hyperparameters are then constrained using observed data through Bayesian inference. This approach has been frequently applied to estimate the population properties of stellar-mass black hole binaries using GW events detected by LIGO/Virgo, such as those reported in the GWTC catalogs (Abbott et al. 2021b,a).

In this subsection, we outline the process of estimating the merger rate of SMBHs and galaxies using hierarchical Bayesian inference.

Given the LISA data $\{\mathbf{d}\}$ of SMBH merger events, the total number of merger events is modeled as an inhomogeneous Poisson process. The corresponding likelihood function is expressed as:

$$\mathcal{L}(\{\mathbf{d}\}|\Lambda) \propto N_{\text{mod}}(\Lambda)^{N_{\text{det}}} e^{-N_{\text{exp}}(\Lambda)} \times \prod_{i=1}^{N_{\text{det}}} \int \mathcal{L}(d_i|\theta) P(\theta|\Lambda) d\theta, \quad (13)$$

where N_{det} is the number of events detected during an observational period T_{det} , $\theta = (m_1, m_2, z_1, z_2, \dots)$ denotes source parameters, Λ refers to the hyperparameters of the merger rate model. $N_{\text{mod}}(\Lambda)$ is the total number of events predicted by the model Λ , while $N_{\text{exp}}(\Lambda) = \xi(\Lambda) N_{\text{mod}}$ represents the expected number of events that could be detected, assuming a detection fraction $\xi(\Lambda)$. $\mathcal{L}(d_i|\theta)$ is the likelihood of an individual GW event d_i , and $P(\theta|\Lambda)$ denotes the population distribution corresponding to model Λ . In this context, the detection fraction $\xi(\Lambda)$ is assumed to be unity, as the SMBH binary merger events in the considered mass and redshift ranges typically have large signal to noise ratios (Amaro-Seoane et al. 2017b).

The integration over θ in the likelihood function of equation (13) can be evaluated by averaging the population distribution $P(\theta|\Lambda)$ over Monte-Carlo (MC) samples of θ_i , which are drawn from the likelihood function $\mathcal{L}(d_i|\theta)$ for each individual event i . This allows the expression to be rewritten as:

$$\mathcal{L}(\{\mathbf{d}\}|\Lambda) \propto N(\Lambda)^{N_{\text{det}}} e^{-N_{\text{exp}}(\Lambda)} \prod_{i=1}^{N_{\text{det}}} \left\langle \frac{P(\theta|\Lambda)}{P_\emptyset(\theta)} \right\rangle, \quad (14)$$

where $\langle \dots \rangle$ is the average over samples of θ_i , and $P_\emptyset(\theta)$ is the default prior taken in the parameter estimation which is usually set to a uniform distribution.

The posterior of the hyperparameters, $P(\Lambda|\{\mathbf{d}\})$, given the data $\{\mathbf{d}\}$, is the multiply of the likelihood $\mathcal{L}(\{\mathbf{d}\}|\Lambda)$ and prior $P(\Lambda)$ of the model

$$P(\Lambda|\{\mathbf{d}\}) \propto \mathcal{L}(\{\mathbf{d}\}|\Lambda) P(\Lambda). \quad (15)$$

Here, we assume a uniform distribution for model prior $P(\Lambda)$.

We consider a population model that describes the joint distribution of two key population properties: the total mass M_\bullet of the SMBH binary and the redshift z at their merger, i.e., $\theta = (M_\bullet, z)$. The corresponding population distribution, $P(\theta|\Lambda)$, is given by the normalized merger rate $\frac{d^2 n_\bullet}{dz d \log_{10} M_\bullet}$ of SMBH binaries (equation (4)), which is defined as:

$$P(\theta|\Lambda) = \frac{1}{N(\Lambda)} \frac{d^2 n_\bullet}{dz d \log_{10} M_\bullet}(M_\bullet, z|\Lambda), \quad (16)$$

where

$$N(\Lambda) = \int \int \frac{d^2 n_\bullet}{dz d M_\bullet}(M_\bullet, z|\Lambda) dM_\bullet dz, \quad (17)$$

is the number of merger events per year (in Earth time). The predicted total number of mergers, $N(\Lambda)$, during an observational period T_{det} , is given by $N(\Lambda) = N(\Lambda) T_{\text{det}}$.

5 INFERRING THE MERGER RATE OF SMBHS AND GALAXIES

In this section we generate mock LISA GW data from different cases of models, and estimate the merger rate of galaxies and SMBHs from the current PTA data and the mock LISA data. We then compare the reconstructed results with observations and theoretical simulations.

5.1 Inferring the Merger Rate of Galaxies

5.1.1 Theoretical Models of Galaxy Merger Rates

The model of SMBH merger rate is determined by equation (4). We further define the galaxy merger rate per galaxy per unit time as

$$\frac{dN}{dt_r}(z, M_* | \Lambda_{\text{dN/dt}}) = n_0 \left(\frac{M_*}{10^{11} M_\odot} \right)^{\alpha_0 + \alpha_1(1+z)} (1+z)^\beta, \quad (18)$$

where t_r is the time measured at the source's rest frame. Then

$$\begin{aligned} \mathcal{R}_{\text{Gal}}(z, M_* | \Lambda_{\text{dN/dt}}) &= \frac{dN}{dt}(z, M_* | \Lambda_{\text{dN/dt}}) \\ &= \frac{1}{(1+z)} \frac{dN}{dt_r}(z, M_* | \Lambda_{\text{dN/dt}}), \end{aligned} \quad (19)$$

is the galaxy merger rate per galaxy per unit time, with t denotes the time measured by earth observer.

We consider two different models for $\frac{dN}{dt_r}$ by setting the model parameters in the following ways:

Case 1: where $\Lambda_{\text{dN/dt}} = \{n_0, \alpha_0, \beta\}$, and $\alpha_1 = 0$. This model is commonly adopted in studies of the PTA SGWB strain generated by SMBH binary populations (e. g., Chen et al. 2019; Antoniadis et al. 2024).

Case 2: where $\Lambda_{\text{dN/dt}} = \{\alpha_0, \alpha_1, \beta\}$, and $n_0 = 0.03$. In this case, the merger rate dN/dt_r with $\alpha_0 = 0.2$, $\alpha_1 = -0.01$, and $\beta = 2.4$ serves as a simplified approximation to the best-fit results predicted by the Illustris simulation (Rodríguez-Gomez et al. 2015) (see Fig. A1 for details). It is worth noting that for $M_* < 10^{11} M_\odot$, a positive value of α_1 acts as an exponential suppression of dN/dt_r at high redshift, as demonstrated by (Duan et al. 2024), where the authors fit the pair fraction and galaxy merger rate using a power-law + exponential model.

5.1.2 Relating the Merger Rate of Galaxies to the Merger Rate of SMBHs

By substituting equation (19) and (5) into equation (4), the merger rate of SMBH binaries can be determined for a given population model Λ . For $z < 4$, we adopt the scaling relationship (equation (3)) based on local observations (Kormendy & Ho 2013), with $a = \log_{10} \kappa + 9 - 11 * b$, $b = 1.17 \pm 0.08$, and $\epsilon = 0.28$, where $\kappa = 0.49^{+0.06}_{-0.05}$. For $z \geq 4$, we adopt the scaling relationship based on recent JWST results (Pacucci & Loeb 2024) with $a = -2.43 \pm 0.83$, $b = 1.06 \pm 0.09$, and $\epsilon = 0.69$. The GSMF (equation (6)) is derived from a series of observations spanning $z = 0 - 10.5$ (Baldry et al. 2012; Huertas-Company et al. 2016; Santini et al. 2012; McLeod et al. 2021; Song et al. 2016; Stefanon et al. 2021). To consider the observational uncertainties of GSMF and $M_\bullet - M_*$ relation in the estimation of model parameters, the parameters Λ_{GSMF} and $\Lambda_{M_\bullet - M_*}$ used in the Likelihood function for parameter estimation are randomly sampled from the parameter space constrained at each observational redshift bin.

In the following sections we assume a unit SMBH occupation fraction for galaxies. Since the lowest mass end of SMBHs we consider in this work is $M_\bullet = 10^5 M_\odot$, the corresponding lower mass bound of galaxies in the scaling relationship is $M_* = 10^7 M_\odot$. This unit occupation fraction assumption represents a rough approximation to the recent multiwavelength constraints reported by Burke et al. (2024), who find a local black hole occupation fraction of at least 90 per cent at a stellar mass of $M_* = 10^8 M_\odot$ and at least 39 per cent at $M_* = 10^7 M_\odot$. We also discuss a varying occupation fraction and the constrains in section 5.4.

5.1.3 Estimating Galaxy Merger Rates Using Mock LISA Data and PTA Observations

Here, we present two realizations of LISA GW events in Fig 2, which displays the mass–redshift distribution of the these events. In both cases, the SMBH binary merger rate is computed using a taken galaxy merger rate model along with specific GSMFs and $M_\bullet - M_*$ relations. The galaxy merger rate per galaxy adopts the same set of model parameters with $n_0 = 0.03$, $\alpha_0 = 0.2$, $\alpha_1 = -0.01$, and $\beta = 2.4$ (see equation (18)). These parameters correspond to the injected values used to generate the mock datasets, which will later be used to constrain the (initially unknown) model parameters. The comparison between this assumption of galaxy merger rate and the ones predicted from cosmological simulations or semi-analytical models (Rodríguez-Gomez et al. 2015; O’Leary et al. 2021; Huško et al. 2022) is illustrated in Fig. A1. The parameters Λ_{GSMF} and $\Lambda_{M_\bullet - M_*}$ in the GSMFs and $M_\bullet - M_*$ relations are randomly sampled from observational constraints across different redshift bins. The corresponding parameter sets for the two realizations, labelled GW(eg1) and GW(eg2), are provided in Tables A1 and A2, respectively. The GW events shown in Fig. 2 are then sampled from the corresponding SMBH binary merger rate. The error bars of mass and redshift in each event is calculated using the Fisher information matrix with the phenomenological waveform model PhenomA (Ajith et al. 2007, 2011). The small error bars reflect LISA’s high signal to noise ratio for these events. The difference of the event number and merger distribution between these two models is due to the different sets of Λ_{GSMF} and $\Lambda_{M_\bullet - M_*}$ from the sampling, rather than the different choices of model parameters, e.g., $\Lambda = \Lambda_{\text{dN/dt}}$. For the current discussion, no delay time between galaxy mergers and SMBH mergers is assumed. The non-vanishing delay time is discussed in subsections 5.2-5.4.

Figs. 3 and 4 present the posterior distributions for the model parameters $\Lambda_{\text{dN/dt}} = \{n_0, \alpha_0, \beta\}$ in Case 1 and $\Lambda_{\text{dN/dt}} = \{\alpha_0, \alpha_1, \beta\}$ in Case 2, as estimated from the two realizations of mock data shown in Fig 2. In each estimation process, we compare the results inferred from the joint (mock) LISA + PTA data (red lines) with those inferred solely from the mock LISA data (gray lines). From the figures, we can see that:

- LISA’s detection of SMBH binary merger events plays a pivotal role in recovering the merger rates of galaxies and SMBHs. Additionally, incorporating PTA constraints on the SGWB strain further enhances the precision of model parameter estimation. This is expected, as LISA-like detectors can effectively measure the merger distribution, such as in the joint mass-redshift distribution discussed here, and fit the data using a hierarchical Bayesian inference approach;
- A larger number of detected events yields tighter constraints on the model parameters. For the model parameters estimated from the first GW mock dataset (left panel of Fig. 2), which contains more events, the injected truth values lie well within the corresponding 1σ credible regions (left panels of Figs. 3 and 4). In contrast, for the model parameters estimated from the second mock GW data (right panel of Fig. 2), which contains fewer events, the injected truth values (n_0 , α_1 , and β) deviate from the 1σ credible regions (right panels of Figs. 3 and 4). The deviations of these parameters from their peaks is attributed to both systematic biases—arising from observational uncertainties in the adopted GSMFs and $M_\bullet - M_*$ relation—and random biases introduced when generating the mock LISA data from theoretical merger rates. The latter may be mitigated if LISA detects a larger number of GW events, as a larger statistical sample more accurately reflects the true merger rate, reducing uncertainties in parameter estimation;

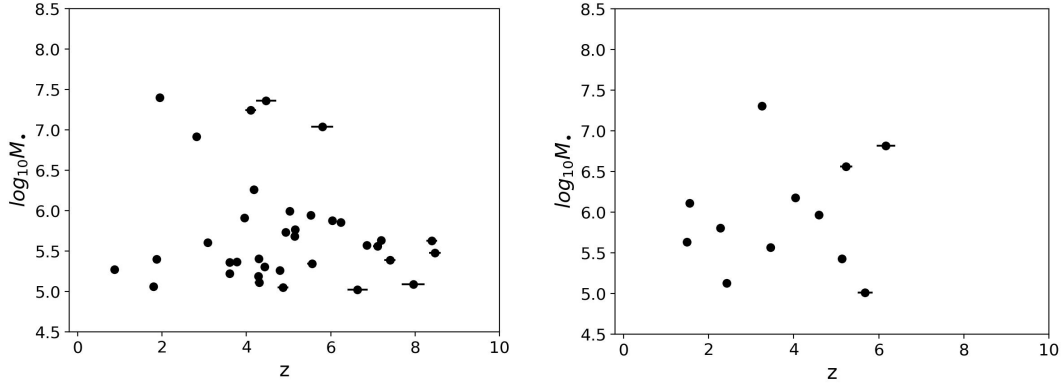


Figure 2. Left: the 36 mock LISA GW events from the first realization. Right: the 12 mock LISA GW events from the second realization.

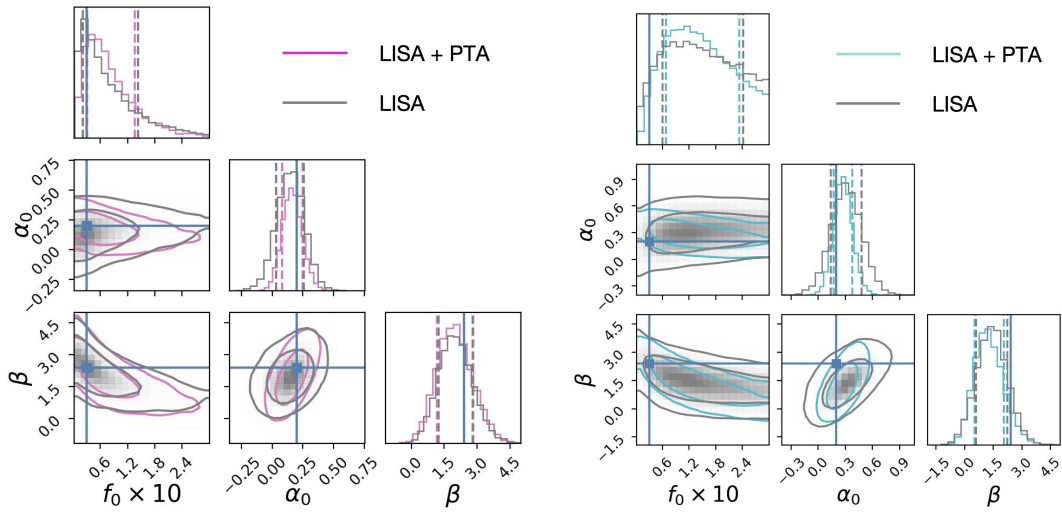


Figure 3. Left: posteriors of the model parameters $\Lambda_{\text{dN/dt}}$ in Case 1 model of galaxy merger rate (discussed in subsection 5.1.1), estimated with mock LISA data from the first realization (left panel of Fig. 2). The pink lines show the result constrained with both LISA mock data and current PTA detection of SGWB (Fig. 1). The gray lines show the result inferred only with LISA mock data. Right: Similar to the left figure, but for the mock LISA data from the second realization (right panel of Fig. 2). In both panels, the horizontal and vertical blue lines represent the injected values.

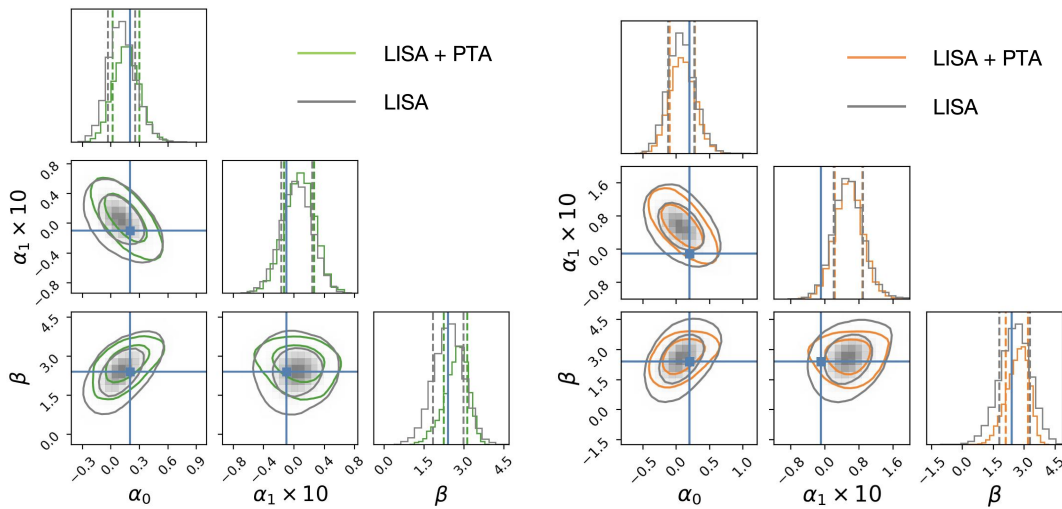


Figure 4. Similar to Fig. 3, but for the Case 2 model of galaxy merger rate discussed in subsection 5.1.1.

c. The model parameters $\{\alpha_0, \alpha_1, \beta\}$ in the Case 2 model are well constrained, whereas the parameter n_0 in the Case 1 model exhibits significant degeneracy, particularly in the second realization, which includes fewer GW events.

5.1.4 Comparing Galaxy Merger Rates Inferred from GWs with Those Derived from Galaxy Pair Observations

The galaxy merger rate, $\frac{dN}{dt}(z)$, could also be observationally derived from studies of galaxy pairs across different redshifts (e.g., Casteels et al. 2014; López-Sanjuan et al. 2015; Duncan et al. 2019b; Conselice et al. 2022; Duan et al. 2024; Puskás et al. 2025) or theoretically predicted using cosmological simulations or semi-analytical models (e.g., Rodríguez-Gomez et al. 2015; O’Leary et al. 2021; Huško et al. 2022). This rate is directly related to the galaxy pair fraction through the following way:

$$\frac{dN}{dt}(z) = \frac{f_p(z, M_*)}{T(z)}, \quad (20)$$

where f_p is the galaxy pair fraction, and T is the merger timescale of the galaxy pairs.

Recently, Duan et al. (2024) conducted a JWST study on galaxy pair fractions and galaxy merger rates, extending the constraints up to $z = 11.5$ (Duan et al. 2024). In their work, the authors found that the galaxy pair fraction, f_p , is better fit to the data using a power-law + exponential parameterization, expressed as:

$$f_p = f_c \times (1+z)^m \times e^{\kappa(1+z)}. \quad (21)$$

The merger timescale T for galaxy pairs in equation (20) could be determined from cosmological simulations.

In Fig. 5, we compare the galaxy merger rate, $\frac{dN}{dt_r}(z)$, as a function of redshift for stellar masses in the range $\log_{10} M_*/M_\odot = [8, 10]$, as recovered from GW detections (pink and cyan lines in the left panel, and green and orange lines in the right panel), to results derived from observations of galaxy pairs (Casteels et al. 2014; López-Sanjuan et al. 2015; Duncan et al. 2019b; Conselice et al. 2022; Duan et al. 2024) (represented by shaped points). Additionally, we compare these results to predictions from the Illustris simulation (Rodríguez-Gomez et al. 2015) (blue lines).

From Fig. 5, we can conclude that:

a. The two different realizations of LISA GW data (Fig. 2) result in distinct estimates of the galaxy merger rate for both Case 1 (pink and cyan lines) and Case 2 (green and orange lines) models. The differences between the two cases become more obvious at higher redshifts, though the associated error bars also increase. Specifically, the galaxy merger rate recovered using the LISA data from the first realization (left panel of Fig. 2) match better with the rates derived from galaxy pair observations for both Case 1 (pink lines) and Case 2 (green lines) models, though the Case 2 model match the data slightly better compared to the Case 1 model in this example. In contrast, the results obtained from the second realization of LISA data (right panel of Fig. 2) for both cases (cyan and orange lines) show a noticeable mismatch with the observationally derived rates at higher redshifts.

b. For the same GW dataset, the reconstructed $2 - \sigma$ confidence regions for the Case 1 and Case 2 merger rate models are largely consistent, except that the Case 1 model generally exhibits larger uncertainties and a systematic bias toward higher values at lower redshifts ($z < 2$), as well as a slight bias toward lower values at higher redshifts ($z > 3$). To test the robustness of the results, we have repeated the recovery of the galaxy merger rate, $\frac{dN}{dt_r}(z)$, for both

Case 1 and Case 2 models using different mock LISA datasets generated by varying the parameters $\{n_0, \alpha_0, \alpha_1, \beta\}$. The results, which are consistent with those shown in Fig. 5, suggest that the observed trends represent general characteristic behaviors of the Case 1 and Case 2 models.

c. The galaxy merger rate, dN/dt , recovered from GW detections can be directly compared to those obtained from electromagnetic observations of galaxy pairs and theoretical simulations. These different and independent methods for deriving the galaxy merger rate serve as a valuable consistency check for one another.

We also repeated the above analysis under the assumption that the $M_\bullet - M_*$ relation remains fixed to its local form (Kormendy & Ho 2013) across the redshifts. The resulting posteriors of the model parameters, estimated from the GW data shown in Figs. 1-2 are presented in Fig. B1. The corresponding galaxy merger rate, $\frac{dN}{dt_r}(z)$, reconstructed from these posteriors, is shown in Fig. B2. Under this assumption, the galaxy merger rates inferred from the two GW datasets in Fig. 2 also diverge at high redshifts, similar to the behavior in Fig. 5, which assumes an $M_\bullet - M_*$ relation at $z > 4$ constrained by JWST observations (Pacucci & Loeb 2024). The primary difference is that Fig. B2 shows systematically higher merger rates with smaller uncertainties at high redshifts compared to Fig. 5. The smaller error bars arise from the smaller uncertainties assumed in the $M_\bullet - M_*$ relation (Kormendy & Ho 2013). The systematically higher inferred merger rates stem from the fact that the local $M_\bullet - M_*$ relation, e.g. Kormendy & Ho (2013), typically predicts smaller SMBH masses compared to those implied by JWST observations (Pacucci & Loeb 2024). As a result, when mapping GSMFs to SMBH number densities via this scaling relation, the local relation yields lower SMBH number densities for a given mass. To reproduce the same GW event distribution, this scenario requires a higher merger rate per SMBH (or per galaxy) to compensate for the reduced number density.

5.2 Inferring the Delay Time Between Galaxy and SMBH Mergers

After galaxy mergers, the SMBHs at the centers of the progenitor galaxies typically undergo an extended evolutionary timescale before coalescing. This delay is primarily governed by the timescale associated with the final parsec evolutionary phase (e.g., Milosavljević & Merritt 2001; Yu 2002; Milosavljević & Merritt 2003). Theoretically, SMBH binaries could merge efficiently via the interaction with environment, e.g., if they reside in a triaxial-shaped stellar distribution environment (e.g., Yu 2002; Merritt & Poon 2004; Holley-Bockelmann & Sigurdsson 2006; Gualandris et al. 2016), a gas-rich environment (e.g., Armitage & Natarajan 2002; Dotti et al. 2006; Haiman et al. 2009), or they went through multiple mergers (e.g., Hoffman & Loeb 2007).

In this subsection, we assess the feasibility of inferring the delay timescale between galaxy mergers and SMBH coalescences using the method proposed in this work. Following the approach described in subsection 5.1.3, we generate mock LISA datasets based on a merger rate model with $\{n_0, \alpha_0, \alpha_1, \beta\} = \{0.03, 0.2, -0.01, 2.4\}$ (see equation (18)), and assume fixed delay times of $\tau = 0.2, 0.5, 1$ Gyr for comparison. These values represent characteristic timescales predicted in scenarios where SMBH binaries harden through interactions with stars in the loss cone of triaxial galaxies (see, e.g., Yu 2002; Khan et al. 2011; Vasiliev et al. 2015). The GSMFs and $M_\bullet - M_*$ relations used at different redshift bins are randomly sampled from observational constraints and listed in Tables A1-A2. The four sets of mock LISA data generated under the

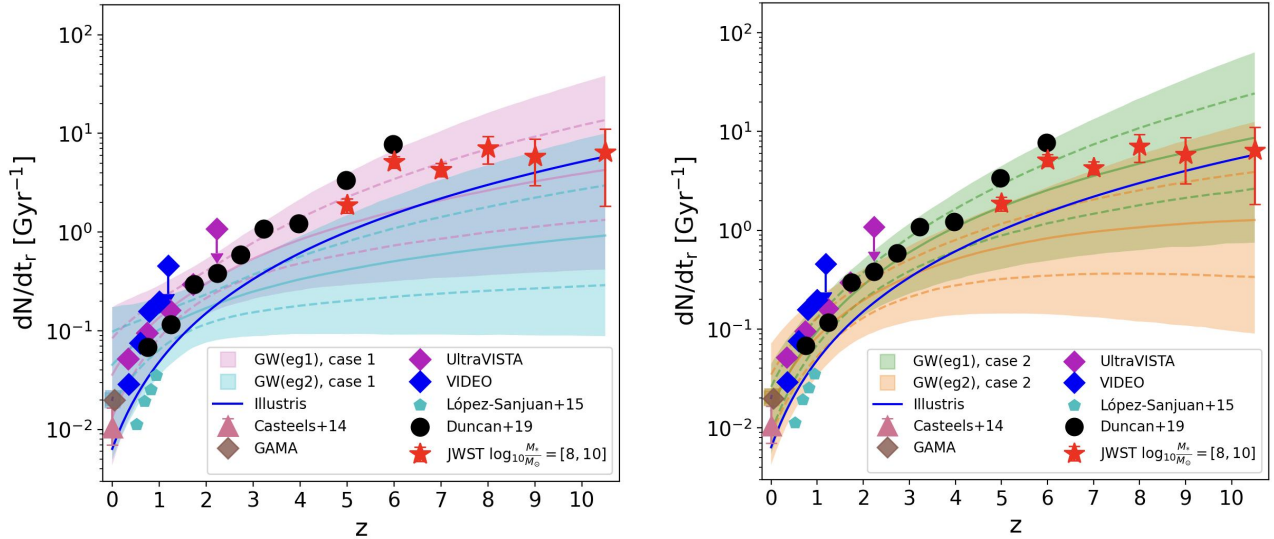


Figure 5. The galaxy merger rate $\frac{dN}{dt_r}(z)$ for galaxy stellar mass in the range $\log_{10} M_*/M_\odot = [8, 10]$. Left panel: The pink (cyan) lines represent the recovered merger rate, $\frac{dN}{dt_r}(z)$, based on the posterior distributions of model parameters presented in the left (right) panel of Fig. 3, using the LISA + PTA data. Right panel: The green (orange) lines represent the recovered merger rate, $\frac{dN}{dt_r}(z)$, based on the posterior distributions of model parameters presented in the left (right) panel of Fig. 4, using the LISA + PTA data. In both panels, the filled regions represent the $2 - \sigma$ confidence interval, the dashed lines represent the corresponding $1 - \sigma$ confidence interval, and the solid (pink and cyan) lines represent the medium values. The shaped points with error bars represent the galaxy merger rates derived from the observations of galaxy pairs across different redshift bins (Casteels et al. 2014; López-Sanjuan et al. 2015; Duncan et al. 2019b; Conselice et al. 2022), in particular, the red stars show the results from recent JWST observations (Duan et al. 2024). We also show the merger rate for galaxy stellar mass in the range $\log_{10} M_*/M_\odot = [8, 10]$ predicted by the Illustris simulation (Rodríguez-Gomez et al. 2015; O’Leary et al. 2021; Huško et al. 2022) in the blue lines.

above assumptions are shown in Fig. 6, where the small error bars in mass and redshift reflect the high signal-to-noise ratios of these events.

The model parameters in this population model of SMBH binary merger rate (equation (4)) is now described by $\Lambda = \{\tau, \Lambda_{dN/dt}\}$, with $\Lambda_{dN/dt} = \{\alpha_0, \alpha_1, \beta\}$. The posteriors of the model parameters inferred from the four sets of mock LISA data (Fig. 6) are shown in subfigures (a)-(d) of Fig. 7 respectively, where the gray lines represent the results inferred from the mock LISA data only, and the red lines correspond to the results obtained by jointly analysing these mock LISA data with the PTA constraints on the SGWB strain. As illustrated in Fig. 7, the delay times in these four examples are properly constrained from the mock LISA data. Incorporating PTA constraints improves parameter estimation by either narrowing the 1σ credible regions or shifting their centres closer to the injected truth values (shown as vertical lines). For some model parameters, the injected values lie near the edges of the 1σ posterior distributions rather than at their peaks. Notably, the injected value $\tau = 0.8$, Gyr in subfigure (c) of Fig. 7 falls outside the 1σ region, while still within the 2σ contour. These deviations can be attributed to both systematic biases—arising from observational uncertainties in the adopted GSMFs and $M_\bullet - M_*$ relation—and random biases introduced when generating the mock LISA data from theoretical merger rates. The latter may be mitigated if LISA detects a larger number of GW events, enabling the event distribution to better reflect the true merger rate. This could be alleviated either through a higher intrinsic merger rate in the LISA frequency band or by extending the mission duration beyond its nominal four-year baseline. The bimodal and subpeak structures observed in the posteriors of the delay time τ in subfigures (a) and (c) arise from a combination of model degeneracies and limited observational constraints.

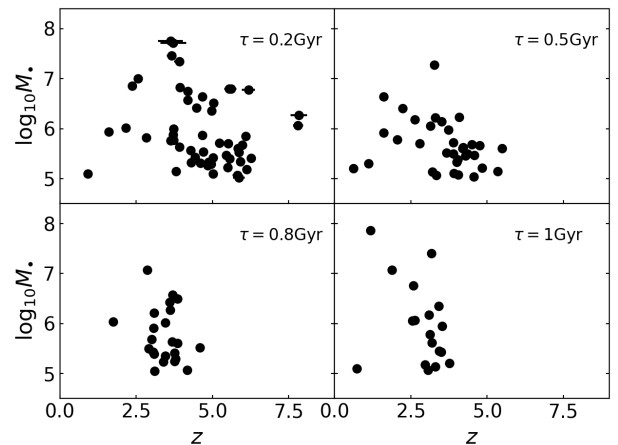


Figure 6. Mock LISA GW data generated assuming a delay time of $\tau = 0.2$ Gyr, 0.5 Gyr, 0.8 Gyr, and 1 Gyr respectively.

In this work, we only consider a constant delay model due to the computational challenges of performing high-dimensional integrations as well as dealing with large model uncertainties (i.e., observational uncertainties from the GSMFs and scaling relations) in the likelihood. While a delay time model with a distribution would be more realistic, it is computationally expensive, prone to convergence issues, and exceeds our current resources. In our previous work (Fang & Yang 2023), we investigated delay-time models with specific distributions while assuming fixed galaxy merger rate model. Future studies should explore distributed delay time models in the framework of this context to provide a more comprehensive understanding of SMBH binary evolution.

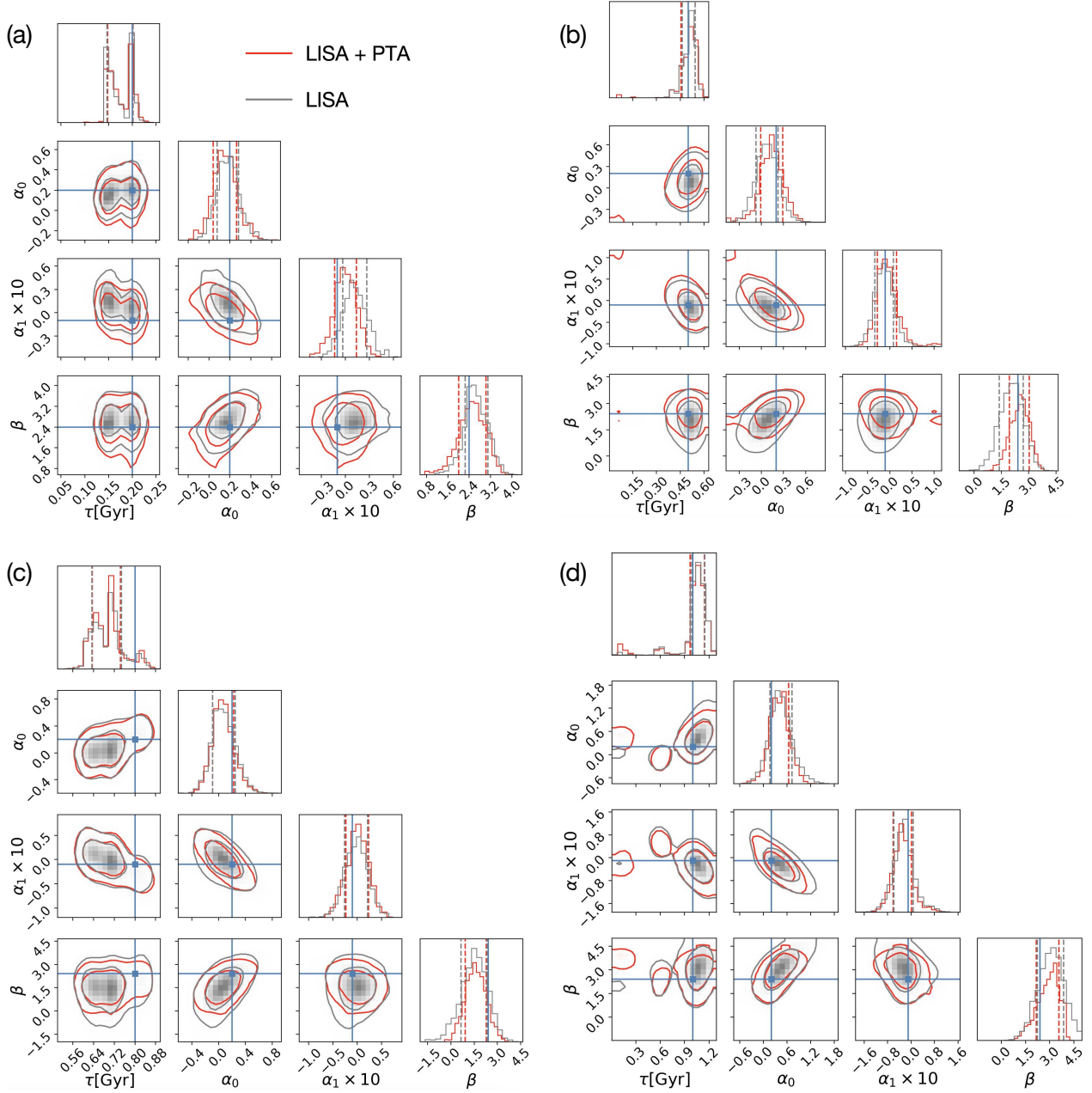


Figure 7. Posterior distributions of the model parameters $\Lambda = \{\tau, \alpha_0, \alpha_1, \beta\}$, inferred from the mock LISA data presented in Fig. 6. Subfigures (a) - (d) show the results for delay times of $\tau = 0.2\text{Gyr}, 0.5\text{Gyr}, 0.8\text{Gyr}$ and 1Gyr , respectively. The horizontal and vertical blue lines represent the injected parameter values.

5.3 Mass Assembly of SMBHs Driven by Mergers

The merger rate of SMBH binaries, $\frac{d^2 n_{\bullet}}{dz dM_{\bullet}}$, can be reconstructed by substituting the posterior distribution values of Λ into equation (4). Using the reconstructed merger rate, one can further derive the mass assembly of SMBHs contributed by mergers, expressed as:

$$\frac{d^2 M_{\bullet}}{dV dt} = \Phi_{\bullet}(M_{\bullet}, z) \mathcal{R}_{\bullet}(M_{\bullet}, z) M_{\bullet} q_{\bullet}, \quad (22)$$

where $M_{\bullet} q_{\bullet}$ is the mass of the secondary SMBH. Since we are considering major mergers, the mass ratio $q_{\bullet} \in [1/4, 1]$. For simplicity, we assume $q_{\bullet} = 0.6$, representing an average value for q_{\bullet} .

Fig. 8 illustrates the contribution of mergers (red shaded region, this work) and accretion (crossed green lines, from Pacucci & Loeb

(2020)) to SMBH mass assembly. The first and second columns of Fig. 8 show that the galaxy merger rates, dN/dt_{r} , in the Case 1 (pink lines and shaded region in Figs. 3 and 5) and Case 2 (green lines and shaded region in Figs. 4 and 5) models produce a similar SMBH merger rate—and hence a similar SMBH mass assembly via mergers—at $z > 2$. However, at $z < 2$, the Case 1 model is biased towards a higher SMBH merger rate compared to the Case 2 model, a trend also reflected in the recovered galaxy merger rates shown in Fig. 5. The merger mass assembly in the first two columns at $z \geq 4$ exhibits large uncertainties, due to the uncertainties in the SMBH mass function propagated from the scaling relationship and GSMFs, and the uncertainties in the estimated galaxy merger rate at this redshift bin.

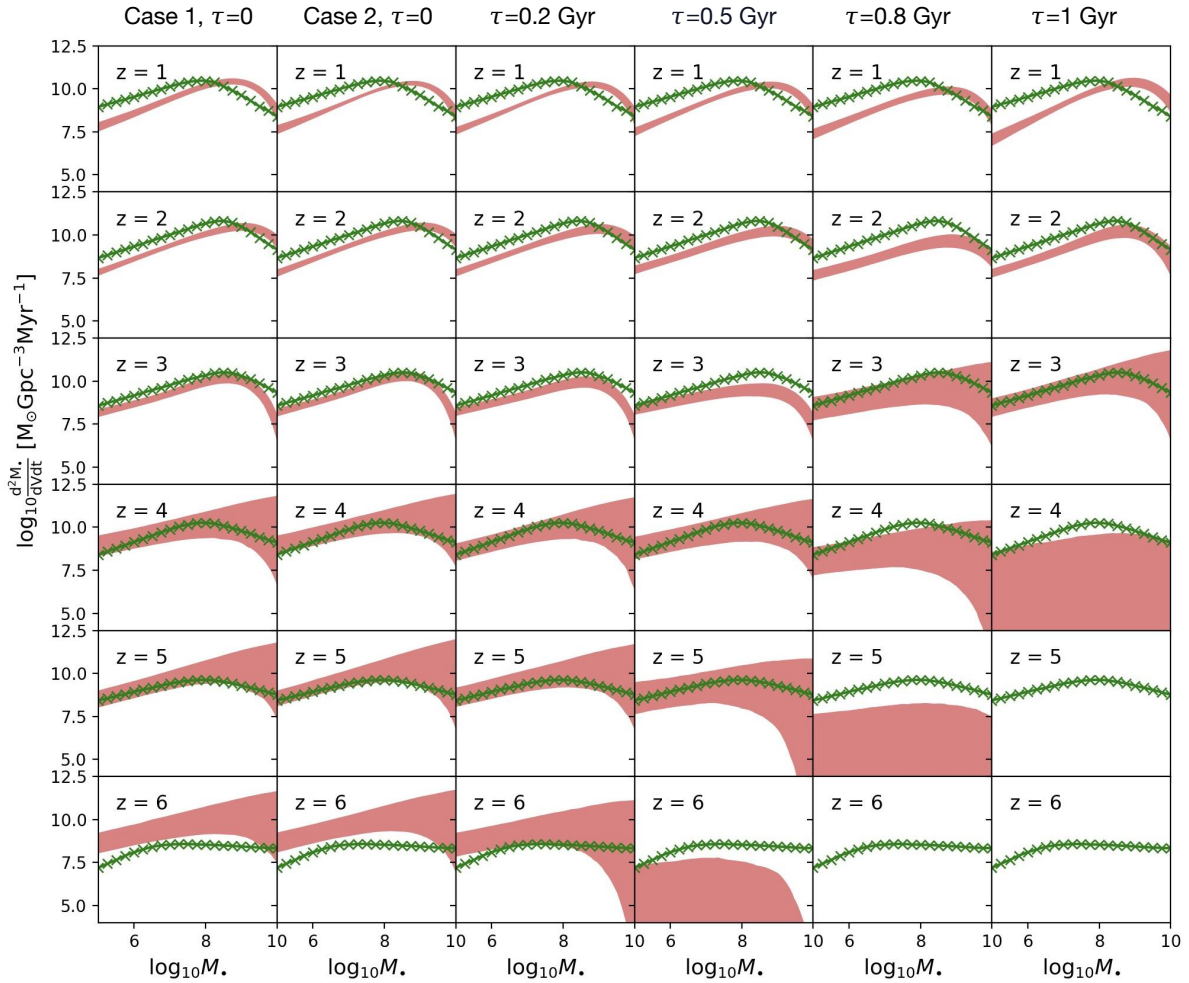


Figure 8. The comparison of the contributions from mergers ($1 - \sigma$ credible region in the red shaded region, this work) and accretion (crossed green lines) to the mass assembly of SMBHs for different redshifts ($z = 1 - 6$) and SMBH mass bins ($\log_{10} M_{\bullet} / M_{\odot} = [5, 10]$). First column: SMBH mass assembly via mergers, derived from the estimated galaxy merger rate assuming the Case 1 model with the first realization of GW data (pink lines and shaded region in Figs. 3 and 5). Second column: Similar to the first column but based on the galaxy merger rate from the Case 2 model (red lines and shaded region in Figs. 4 and 5). Third to sixth columns: Similar to the first two columns but based on the model assuming a delay time of $\tau = 0.2\text{Gyr}$, 0.5Gyr , 0.8Gyr , and 1Gyr respectively (red lines in subfigures (a)-(d) of Fig. 7). The crossed green lines represent the SMBH mass assembly contributed by accretion, based on the simulation conducted by (Pacucci & Loeb 2020).

The delay time of SMBH binary mergers will have a negative impact on their merger rate/merger assembly, as illustrated by the comparison between the cases with delay (third to sixth columns) and without delay (first and second columns) in Fig. 8. The suppression becomes more pronounced with increasing delay time, leading to a steeper decline in the SMBH merger rate at high redshift (e.g., $z > 4$ in the last four columns). In particular, the complete absence of mergers at $z \geq 6$ and $z \geq 5$ in the fifth and sixth columns, respectively, arises from the assumed delay times of $\tau = 0.8\text{Gyr}$ and 1Gyr in the corresponding models.

By comparing the contributions to SMBH mass assembly from mergers and accretion, one can assess which process dominates SMBH growth across different redshifts. As shown in Fig. 8, accretion generally dominates the mass assembly at $z < 3$ for all the considered models, except for the most massive SMBHs ($\log_{10} M_{\bullet} / M_{\odot} > 8$ or 9) at lower redshifts ($z \lesssim 1-2$). At higher redshifts ($z \gtrsim 4-5$), mergers become the dominant growth channel when the delay time is short ($\tau \leq 0.2\text{Gyr}$), whereas accretion

overtakes mergers for longer delays ($\tau \geq 0.5\text{Gyr}$). This trend is consistent with the findings of the BRAHMA simulation (Bhowmick et al. 2024), which also shows that mergers dominate early SMBH growth when the merger delay timescale is short.

5.4 SMBH Occupation Fraction of Galaxies

The occupation fraction refers to the proportion of galaxies that host a SMBH at their centers. It encodes key information about the formation and evolution of SMBHs and directly impacts the expected rate of SMBH mergers, influencing predictions for GW signals detectable by LISA. Observations in the local universe indicate that nearly all massive galaxies contain SMBHs (e.g., Kormendy & Ho 2013), while the occupation fraction in low-mass dwarf galaxies remains uncertain (e.g., Miller et al. 2015; Burke et al. 2024; Greene et al. 2020). Constraining the occupation fraction in dwarf galaxies is critical for distinguishing between different SMBH seed formation scenarios (e.g., Natarajan 2014; Inayoshi et al. 2020).

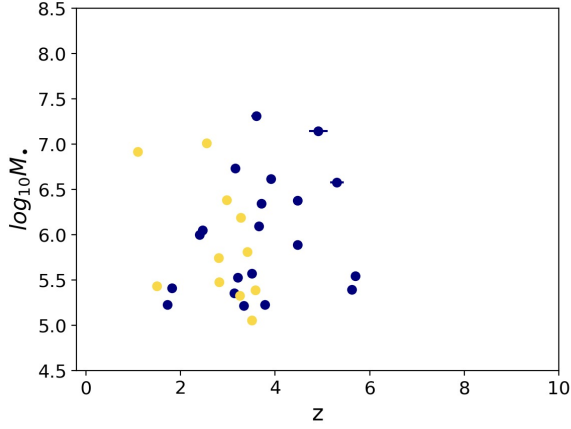


Figure 9. Mock LISA data realized from merger rate model assuming $\{\tau, f_3, \alpha_0, \alpha_1, \beta\} = \{0.5\text{Gyr}, 0.46, 0.2, -0.01, 2.4\}$ (navy) and $\{\tau, f_3, \alpha_0, \alpha_1, \beta\} = \{1\text{Gyr}, 0.46, 0.2, -0.01, 2.4\}$ (gold) respectively, and the GSMF and $M_\bullet - M_*$ relationship are set to Tables A1-A2.

In the previous sections, we have assumed a unit occupation fraction (for those galaxies corresponding to SMBHs with masses above $10^5 M_\odot$ in the scaling relationship), which is a rough approximation to the recent multiwavelength constraints reported by [Burke et al. \(2024\)](#). To further investigate the potential of gravitational-wave detections to constrain the occupation fraction for galaxy with low stellar mass, we adopt a mass-dependent parameterization of occupation fraction f_{occ} following equation (3) of [Beckmann et al. \(2023\)](#) and [Langen et al. \(2025\)](#), which writes,

$$f_{\text{occ}} = 1 - \frac{f_i}{1 + \left(\frac{\log_{10}(M_*)}{M_i^*}\right)^{\epsilon_i}}, \quad (23)$$

where the parameters $\{f_i, M_i^*, \epsilon_i\}$ at $z < 1$, $1 \leq z < 2$, and $2 \leq z < 3$ are assigned the corresponding values at $z = 0.25$, 1, and 2 respectively, as listed in Table 1 of [Beckmann et al. \(2023\)](#). For $z \geq 3$, we follow a similar treatment in [Langen et al. \(2025\)](#) by fixing $M_3^* = 8.55$ and $\epsilon_3 = 33.75$ while keep f_3 as free parameter. The value of occupation fraction f_{occ} at the low-mass end of M_* at high redshift ($z \geq 3$) is primarily determined by f_3 . Constraining f_3 therefore plays an important role in probing the formation of SMBH seeds.

We extend the set of model parameters Λ by including the occupation parameter f_3 , such that $\Lambda = \{\tau, f_3, \Lambda_{\text{dN/dt}}\}$, with $\Lambda_{\text{dN/dt}} = \{\alpha_0, \alpha_1, \beta\}$, and jointly constrain them using mock LISA data in combination with PTA limits on the SGWB. Similar to the previous procedure, we generate two sets of mock LISA data assuming $\{f_3, \tau, n_0, \alpha_0, \alpha_1, \beta\} = \{0.46, 0.5\text{Gyr}, 0.03, 0.2, -0.01, 2.4\}$ (navy) and $\{0.46, 1\text{Gyr}, 0.03, 0.2, -0.01, 2.4\}$ (gold), respectively. In both cases, the GSMF and $M_\bullet - M_*$ relation are randomly sampled within observational constraints as listed in Tables A1-A2. The resulting posterior distributions of the model parameters are shown in Fig. 10. We find that in both scenarios, the parameter f_3 remains poorly constrained, whereas the other parameters, τ and $\Lambda_{\text{dN/dt}}$, are well determined. The flat posterior of f_3 arises from its strong degeneracy with the delay time and the galaxy merger rate (at $z > 3$). Although the model is sensitive to f_3 at $z > 3$ when τ and $\Lambda_{\text{dN/dt}}$ are fixed, the presence of strong degeneracies implies that the model primarily responds to specific combinations of these parameters rather than to f_3 individually.

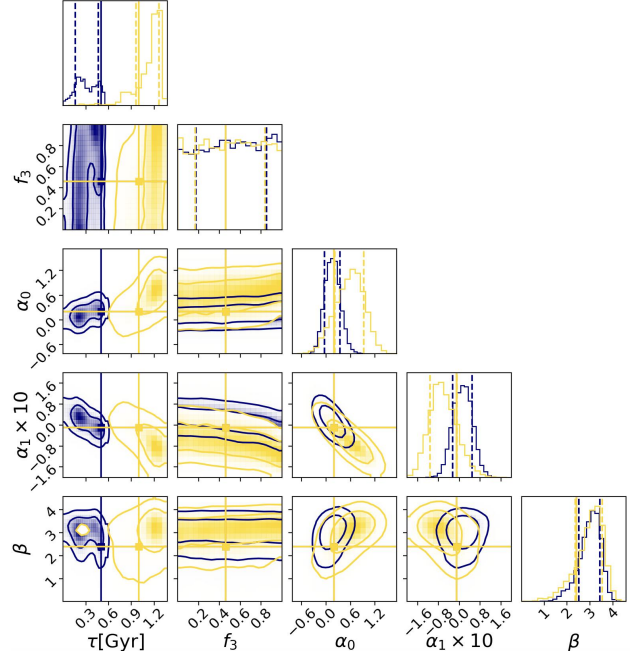


Figure 10. Posteriors of model parameters $\Lambda = \{\tau, f_3, \alpha_0, \alpha_1, \beta\}$, inferred from the mock LISA data shown in Fig. 9, assuming delay time of $\tau = 0.5\text{Gyr}$ (navy) and 1Gyr (gold). The inner and outer lines show the 0.68 and 0.954 levels. The horizontal and vertical lines represent the corresponding injected parameter values.

6 CONCLUSION AND DISCUSSION

This work investigates the merger rate of SMBHs and their host galaxies using SGWB detections from PTAs and mock GW data for LISA-like detectors. The findings highlight the critical role of GW detections with LISA-like detectors together with PTAs in exploring the galaxy/SMBH mergers in the hierarchical assembly and the mass growth of SMBHs. By incorporating observational constraints from the $M_\bullet - M_*$ relation ([Kormendy & Ho 2013](#); [Pacucci & Loeb 2024](#)) and GSMFs ([Baldry et al. 2012](#); [Huertas-Company et al. 2016](#); [Santini et al. 2012](#); [McLeod et al. 2021](#); [Song et al. 2016](#); [Stefanon et al. 2021](#)), this study provides a framework for estimating the merger rate of SMBHs and their host galaxies.

The PTAs and LISA-like detectors provide complementary windows into the SMBH merger process. The current PTAs provide a piece of evidence of a SGWB ([Agazie et al. 2023](#); [Antoniadis et al. 2023a,b](#); [Reardon et al. 2023](#); [Xu et al. 2023](#)), which is most likely to be sourced by SMBH binaries of mass $10^8 - 10^9 M_\odot$ dominated by redshift $z < 3$. The future LISA-like detector is capable of detecting SMBH binary merger events at higher redshifts ($z = 20 - 30$) and wide mass range of SMBHs ($10^5 - 10^8 M_\odot$). The results demonstrate that LISA's detection of SMBH binary mergers is crucial for reconstructing merger rates (Fig. 3-5), the delay time of SMBH binary mergers (Fig. 7), and revealing the contribution of mergers to SMBH growth (Fig. 8). Moreover, incorporating PTA constraints on the SGWB further refines model parameters, reducing uncertainties.

A key outcome of this study is the ability to compare galaxy merger rate at different redshift bins inferred from GW detections with those obtained from galaxy pair observations (e.g. [Casteels et al. 2014](#); [López-Sanjuan et al. 2015](#); [Duncan et al. 2019b](#); [Conselice et al. 2022](#); [Duan et al. 2024](#)) and cosmological simulations (e.g. [Rodríguez-Gomez et al. 2015](#)) (seeing Fig. 5 for details). GW de-

tections provide independent approaches to estimating galaxy merger rates and thus serve as a valuable cross-check for one another. Our analysis using mock LISA data indicates that the number of detected events and their joint distribution in mass and redshift are crucial for constraining galaxy and SMBH merger rates. Specifically, GW data with 36 events yield results consistent with galaxy pair observations, whereas data with only 12 events fail to capture the high-redshift behavior. At higher redshift, larger biases emerge due to the limited number of detections and increased uncertainties in the GSMFs and the $M_{\bullet}-M_{*}$ relations.

SMBHs assemble their mass through mergers and accretion. The comparison between these two processes could reveal the mass assembly histories of SMBHs. In our analysis (Fig. 8), the recovered merger mass assembly at high redshift (particularly at $z \geq 4$) exhibits significant uncertainties, this is mainly caused by the uncertainties in the SMBH mass function propagated from the $M_{\bullet}-M_{*}$ relation and GSMFs, as well as the uncertainties in the estimated galaxy merger rate at such redshift bin. Future observations providing more robust constraints on the $M_{\bullet}-M_{*}$ relation and GSMFs at high redshifts will help reduce these uncertainties. The delay time between galaxy mergers and subsequent SMBH coalescences suppresses the SMBH merger rate and can significantly affect the contribution of mergers to the growth of SMBHs. Our analysis (Fig. 8) shows that in models with short or vanishing delay times ($\tau \leq 0.2$ Gyr), mergers typically dominate SMBH mass assembly at high redshifts ($z > 4$). In contrast, for models with delay times longer than 0.5 Gyr (0.8 Gyr), accretion becomes the primary driver of SMBH mass growth beyond $z \sim 6$ (4).

We further examine the estimation of the SMBH occupation fraction in galaxies at $z > 3$ (f_3), parameterized similarly to Beckmann et al. (2023) and Langen et al. (2025), in conjunction with the delay time and galaxy merger rate parameters (Fig. 10). While the delay time and merger rate parameters are well constrained, f_3 remains poorly determined. Its flat posterior distribution reflects its significant degeneracies with both the delay time and the galaxy merger rate. The delay time parameter is properly constrained (Figs. 7 and 10), consistent with our previous findings (Fang & Yang 2023), where both power-law and Gaussian delay time distributions could be recovered. In this work, due to computational limitations, we restrict our analysis to a constant delay model. Future studies in this framework should explore more realistic delay time models described by distribution functions to better capture the complexities of SMBH merger dynamics.

In summary, this study demonstrates the strengths and limitations of combining GW detections with observational constraints on scaling relations and GSMFs to investigate galaxy and SMBH merger rates, estimate the coalescence time of SMBH binaries and its role in the SMBH mass assembly through mergers, and constrain the SMBH occupation fraction in galaxies. Future advancements in GW observatories, such as LISA (Seoane et al. 2013; Amaro-Seoane et al. 2017a), Taiji (Hu & Wu 2017), Tianqin (Luo et al. 2016), and PTAs (Agazie et al. 2023; Antoniadis et al. 2023a,b; Reardon et al. 2023; Xu et al. 2023), alongside improved electromagnetic observations from JWST (e.g. Schneider et al. 2023; Matthee et al. 2024), ngEHT (e.g. D’Orazio & Loeb 2018; Fang & Yang 2022; Johnson et al. 2023) and other facilities will provide deeper insights into the formation and coevolution of SMBHs and their host galaxies. These efforts will ultimately enhance our understanding of the large-scale structure of the universe and the role of SMBH/galaxy mergers in shaping their evolution.

ACKNOWLEDGEMENTS

We acknowledge the use of the HPC Cluster of the National Supercomputing Center in Beijing. This work makes use of the open-sourced python package emcee (Foreman-Mackey et al. 2013). We thank Youjun Lu and Yunfeng Chen for useful discussions. We also thank the anonymous referee for the constructive suggestions that helped improve the quality of this work. YF is supported by the National Natural Science Foundation of China (Grant No. 12405068) and the Start-up Research Fund Project at Ningbo University. RGC is supported by the National Natural Science Foundation of China with Grant No. 12235019.

DATA AVAILABILITY

Data is available upon reasonable request from the authors.

REFERENCES

- Abbott R., et al., 2021a
 Abbott R., et al., 2021b, *ApJL*, 913, L7
 Agazie G., et al., 2023, *ApJL*, 951, L8
 Ajith P., et al., 2007, *Class. Quantum Grav.*, 24, S689
 Ajith P., et al., 2011, *Phys. Rev. Lett.*, 106, 241101
 Amaro-Seoane P., et al., 2017a, *arXiv e-prints*, p. [arXiv:1702.00786](https://arxiv.org/abs/1702.00786)
 Amaro-Seoane P., et al., 2017b, *arXiv e-prints*, p. [arXiv:1702.00786](https://arxiv.org/abs/1702.00786)
 Antoniadis J., et al., 2023a, *A&A*, 678, A48
 Antoniadis J., et al., 2023b, *A&A*, 678, A50
 Antoniadis J., et al., 2024, *A&A*, 685, A94
 Armitage P. J., Natarajan P., 2002, *ApJ*, 567, L9
 Baldry I. K., et al., 2012, *MNRAS*, 421, 621
 Barausse E., 2012, *MNRAS*, 423, 2533
 Beckmann R. S., et al., 2023, *MNRAS*, 523, 5610
 Begelman M. C., Blandford R. D., Rees M. J., 1980, *Nature*, 287, 307
 Bhowmick A. K., et al., 2024, *MNRAS*, 533, 1907
 Bi Y.-C., Wu Y.-M., Chen Z.-C., Huang Q.-G., 2023, *Sci. China Phys. Mech. Astron.*, 66, 120402
 Bogdan A., et al., 2024, *Nature Astron.*, 8, 126
 Burke C. J., Natarajan P., Baldassare V. F., Geha M., 2024, *ApJ*, 978, 77
 Callegari S., Mayer L., Kazantzidis S., Colpi M., Governato F., Quinn T., Wadsley J., 2009, *ApJL*, 696, L89
 Casteels K. R. V., et al., 2014, *MNRAS*, 445, 1157
 Chapon D., Mayer L., Teyssier R., 2013, *MNRAS*, 429, 3114
 Chen S., Sesana A., Conselice C. J., 2019, *MNRAS*, 488, 401
 Chen Y., Yu Q., Lu Y., 2023, *ApJ*, 955, 132
 Conselice C. J., Mundy C. J., Ferreira L., Duncan K., 2022, *ApJ*, 940, 168
 Ding X., et al., 2023, *Nature*, 621, 51
 Dotti M., Colpi M., Haardt F., 2006, *MNRAS*, 367, 103
 Duan Q., et al., 2024, *arXiv e-prints*, p. [arXiv:2407.09472](https://arxiv.org/abs/2407.09472)
 Duncan K., et al., 2019a, *ApJ*, 876, 110
 Duncan K., et al., 2019b, *ApJ*, 876, 110
 D’Orazio D. J., Loeb A., 2018, *ApJ*, 863, 185
 Escala A., Larson R. B., Coppi P. S., Mardones D., 2005, *ApJ*, 630, 152
 Fang Y., Yang H., 2022, *ApJ*, 927, 93
 Fang Y., Yang H., 2023, *MNRAS*, 523, 5120
 Ferrarese L., Merritt D., 2000, *ApJ*, 539, L9
 Foreman-Mackey D., Hogg D. W., Lang D., Goodman J., 2013, *PASP*, 125, 306
 Gebhardt K., et al., 2000, *ApJL*, 539, L13
 Greene J. E., Strader J., Ho L. C., 2020, *ARA&A*, 58, 257
 Gualandris A., Read J. I., Dehnen W., Bortolas E., 2016, *MNRAS*, 464, 2301
 Haiman Z., Kocsis B., Menou K., 2009, *ApJ*, 700, 1952
 Harikane Y., et al., 2023, *ApJ*, 959, 39
 Hoffman L., Loeb A., 2007, *MNRAS*, 377, 957
 Holley-Bockelmann K., Sigurdsson S., 2006

- Hopkins P. F., Hernquist L., Cox T. J., Matteo T. D., Robertson B., Springel V., 2006, *ApJS*, 163, 1
- Hu W.-R., Wu Y.-L., 2017, *Nat. Sci. Rev.*, 4, 685
- Huertas-Company M., et al., 2016, *MNRAS*, 462, 4495
- Huško F., Lacey C. G., Baugh C. M., 2022, *MNRAS*, 509, 5918
- Inayoshi K., Visbal E., Haiman Z., 2020, *ARA&A*, 58, 27
- Johnson M. D., et al., 2023, *Galaxies*, 11, 61
- Katz M. L., Kelley L. Z., Dosopoulou F., Berry S., Blecha L., Larson S. L., 2019, *MNRAS*, 491, 2301
- Khan F. M., Just A., Merritt D., 2011, *ApJ*, 732, 89
- Klein A., et al., 2016, *Phys. Rev. D*, 93, 024003
- Kocevski D. D., et al., 2023, *ApJ*, 954, L4
- Kormendy J., Ho L. C., 2013, *ARA&A*, 51, 511
- Langen V., Tamanini N., Marsat S., Bortolas E., 2025, *MNRAS*, 536, 3366
- Larson R. L., et al., 2023, *ApJ*, 953, L29
- Li J., et al., 2024, *arXiv e-prints*, p. [arXiv:2403.00074](https://arxiv.org/abs/2403.00074)
- López-Sanjuan C., et al., 2015, *A&A*, 576, A53
- Luo J., et al., 2016, *Class. Quantum Grav.*, 33, 035010
- Maiolino R., et al., 2023
- Marconi A., Risaliti G., Gilli R., Hunt L. K., Maiolino R., Salvati M., 2004, *MNRAS*, 351, 169
- Matt C., Gültekin K., Simon J., 2023, *MNRAS*, 524, 4403
- Matthee J., et al., 2024, *arXiv preprint arXiv:2412.02846*
- Mayer L., Kazantzidis S., Madau P., Colpi M., Quinn T. R., Wadsley J., 2007, *Science*, 316, 1874
- McLeod D. J., McLure R. J., Dunlop J. S., Cullen F., Carnall A. C., Duncan K., 2021, *MNRAS*, 503, 4413
- Merritt D., Poon M. Y., 2004, *ApJ*, 606, 788
- Miller B. P., Gallo E., Greene J. E., Kelly B. C., Treu T., Woo J.-H., Baldassare V., 2015, *ApJ*, 799, 98
- Milosavljević M., Merritt D., 2001, *ApJ*, 563, 34
- Milosavljević M., Merritt D., 2003, in Centrella J. M., ed., *American Institute of Physics Conference Series Vol. 686, The Astrophysics of Gravitational Wave Sources*. pp 201–210 ([arXiv:astro-ph/0212270](https://arxiv.org/abs/astro-ph/0212270)), [doi:10.1063/1.1629432](https://doi.org/10.1063/1.1629432)
- Natarajan P., 2014, *Gen. Relativ. Gravit.*, 46, 1702
- O’Leary J. A., Moster B. P., Naab T., Somerville R. S., 2021, *MNRAS*, 501, 3215
- Pacucci F., Loeb A., 2020, *ApJ*, 895, 95
- Pacucci F., Loeb A., 2024, *ApJ*, 964, 154
- Pacucci F., Nguyen B., Carniani S., Maiolino R., Fan X., 2023, *ApJL*, 957, L3
- Pfister H., Lupi A., Capelo P. R., Volonteri M., Bellovary J. M., Dotti M., 2017, *MNRAS*, 471, 3646
- Puskás D., et al., 2025, *arXiv e-prints*, p. [arXiv:2502.01721](https://arxiv.org/abs/2502.01721)
- Reardon D. J., et al., 2023, *ApJL*, 951, L6
- Rodríguez-Gomez V., et al., 2015, *MNRAS*, 449, 49
- Ruan W.-H., Guo Z.-K., Cai R.-G., Zhang Y.-Z., 2018, *arXiv e-prints*, p. [arXiv:1807.09495](https://arxiv.org/abs/1807.09495)
- Santini P., et al., 2012, *A&A*, 538, A33
- Sayeb M., Blecha L., Kelley L. Z., Gerosa D., Kesden M., Thomas J., 2021, *MNRAS*, 501, 2531
- Schneider R., Valiante R., Trinca A., Graziani L., Volonteri M., Maiolino R., 2023, *MNRAS*, 526, 3250
- Seoane P. A., et al., 2013
- Sesana A., 2013a, *MNRAS*, 433, 1
- Sesana A., 2013b, *MNRAS Lett.*, 433, L1
- Sesana A., Volonteri M., Haardt F., 2007, *MNRAS*, 377, 1711
- Sesana A., Vecchio A., Volonteri M., 2009, *MNRAS*, 394, 2255
- Shankar F., et al., 2016, *MNRAS*, 460, 3119
- Simon J., 2023, *ApJL*, 949, L24
- Simon J., Burke-Spolaor S., 2016, *ApJ*, 826, 11
- Soltan A., 1982, *MNRAS*, 200, 115
- Song M., et al., 2016, *ApJ*, 825, 5
- Stefanon M., Bouwens R. J., Labbé I., Illingworth G. D., Gonzalez V., Oesch P. A., 2021, *ApJ*, 922, 29
- Stone M. A., Lyu J., Rieke G. H., Alberts S., Hainline K. N., 2024, *ApJ*, 964, 90
- Taylor L., et al., 2022, *ApJ*, 939, 90
- Übler H., et al., 2023, *A&A*, 677, A145
- Valiante R., et al., 2021, *MNRAS*, 500, 4095
- Vasiliev E., Antonini F., Merritt D., 2015, *ApJ*, 810, 49
- Volonteri M., 2012, *Science*, 337, 544
- Volonteri M., Natarajan P., 2009, *MNRAS*, 400, 1911
- Volonteri M., Haardt F., Madau P., 2003, *ApJ*, 582, 559
- Xu H., et al., 2023, *Res. Astron. Astrophys.*, 23, 075024
- Yu Q., 2002, *MNRAS*, 331, 935
- Yue M., et al., 2024, *ApJ*, 966, 176

APPENDIX A: SETTINGS OF MERGER RATE MODEL FOR GENERATING MOCK GW DATA

In the appendix, we detail the settings of the merger rate model used to generate the mock GW data discussed in Sections 5.1.3, 5.2, and 5.4. Specifically, Fig. A1 shows the galaxy merger rate per galaxy assumed in our model, alongside a comparison with predictions from the simulations in Illustris (Rodríguez-Gomez et al. 2015), GALFORM (Huško et al. 2022), and EMERGE (O’Leary et al. 2021). The GSMFs and $M_{\bullet} - M_{*}$ relation at different redshift bins are sampled from observational constraints, as listed in Tables. A1 and A2.

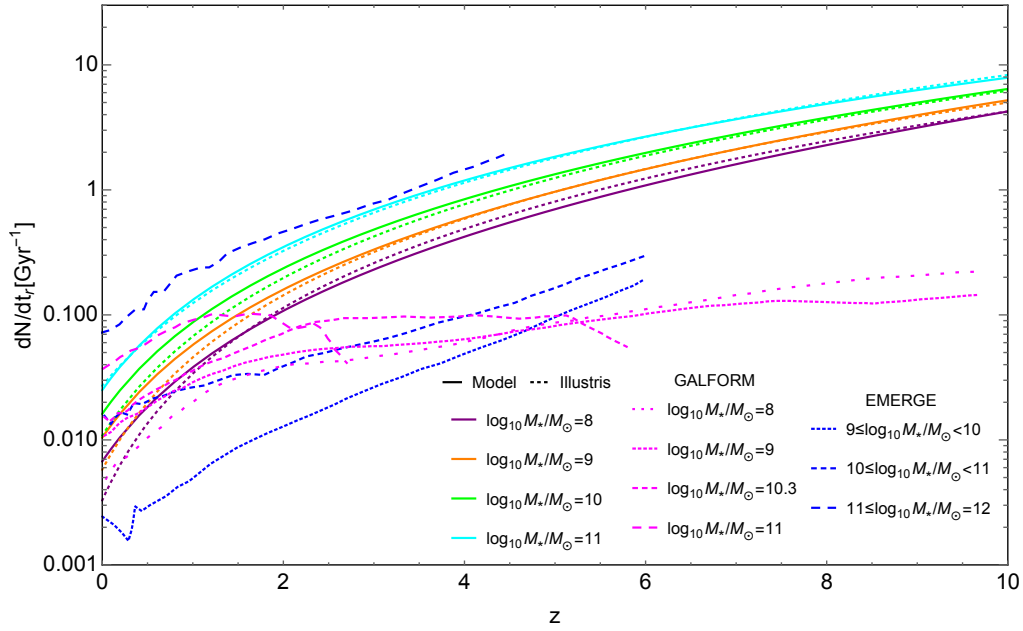


Figure A1. Galaxy merger rates per galaxy assumed in our model for generating the mock LISA GW data (solid lines), compared with predictions from the Illustris simulations (colored dashed lines, (Rodríguez-Gomez et al. 2015)), GALFORM (magenta dashed lines, (Huško et al. 2022)), and EMERGE (blue dashed lines, (O’Leary et al. 2021)).

Table A1. Parameters $[\mathcal{M}_\star, \log_{10} \phi_1, a_1, \log_{10} \phi_2, a_2]$ of the galaxy stellar mass function (equation 6) across different redshift bins, sampled from observational constraints. These values are used to generate the mock LISA data discussed in Sections 5.1.3, 5.2, and 5.4.

Redshift	GW example	$[\mathcal{M}_\star, \log_{10} \phi_1, a_1, \log_{10} \phi_2, a_2]$	bins of redshift
$0 < z \leq 3.5$ (Baldry et al. 2012; Santini et al. 2012) (Huertas-Company et al. 2016) (McLeod et al. 2021)	Sections 5.1.3, 5.2, 5.4	$[[10.66, -2.40, -0.35, -3.10, -1.47],$	$[0 < z \leq 0.2,$
		$[10.86, -2.65, -0.82, -3.35, -1.60],$	$0.2 < z \leq 0.8,$
		$[11.03, -2.88, -1.25, -\text{inf}, 0],$	$0.8 < z \leq 1.1,$
		$[11.32, -3.41, -1.42, -\text{inf}, 0],$	$1.1 < z \leq 2.0,$
		$[10.77, -3.18, -0.68, -3.84, -1.73],$	$2.0 < z \leq 3.0,$
		$[10.84, -3.94, -1.79, -4.3, 0]]$	$3.0 < z \leq 3.5]$
$3.5 < z \leq 10.5$ (Song et al. 2016) (Stefanon et al. 2021)	Section 5.1.3, GW (eg1)	$[[10.77, -3.78, -1.59, -\text{inf}, 0],$	
		$[11.08, -4.20, -1.61, -\text{inf}, 0],$	
		$[10.45, -4.45, -1.82, -\text{inf}, 0],$	
		$[10.17, -4.27, -1.83, -\text{inf}, 0],$	
		$[10.82, -4.74, -1.38, -\text{inf}, 0],$	
		$[9.50, -5.18, -2.00, -\text{inf}, 0],$	
		$[9.50, -6.52, -2.00, -\text{inf}, 0]]$	
$3.5 < z \leq 10.5$ (Song et al. 2016) (Stefanon et al. 2021)	Section 5.1, GW (eg2)	$[[10.91, -3.87, -1.55, -\text{inf}, 0],$	$[3.5 < z \leq 4.5,$
		$[10.66, -4.07, -1.65, -\text{inf}, 0],$	$4.5 < z \leq 5.5,$
		$[9.90, -3.94, -1.80, -\text{inf}, 0],$	$5.5 < z \leq 6.5,$
		$[10.47, -5.27, -2.03, -\text{inf}, 0],$	$6.5 < z \leq 7.5,$
		$[9.42, -4.05, -1.83, -\text{inf}, 0],$	$7.5 < z \leq 8.5,$
		$[9.50, -5.05, -2.00, -\text{inf}, 0],$	$8.5 < z \leq 9.5,$
		$[9.50, -6.26, -2.00, -\text{inf}, 0]]$	$9.5 < z \leq 10.5]$
$3.5 < z \leq 10.5$ (Song et al. 2016) (Stefanon et al. 2021)	Sections 5.2, 5.4	$[[10.66, -3.72, -1.61, -\text{inf}, 0],$	
		$[11.07, -4.23, -1.65, -\text{inf}, 0],$	
		$[10.58, -4.50, -1.80, -\text{inf}, 0],$	
		$[10.29, -4.24, -1.67, -\text{inf}, 0],$	
		$[8.87, -2.85, -0.77, -\text{inf}, 0],$	
		$[9.50, -5.21, -2.00, -\text{inf}, 0],$	
		$[9.50, -5.79, -2.00, -\text{inf}, 0]]$	

Table A2. Parameters $[a, b, \epsilon]$ of the $M_{\bullet} - M_{*}$ relationship (equation (3)), sampled from observational constraints, used in generating the mock LISA data discussed in Sections 5.1.3, 5.2, and 5.4.

Redshift	GW example	$[a, b, \epsilon]$
$0 < z \leq 4$ (Kormendy & Ho 2013)	Section 5.1.3, GW (eg1)	[-5.36, 1.28, 0.28]
	Section 5.1.3, GW (eg2)	[-6.10, 1.35, 0.28]
	Sections 5.2, 5.4	[-4.25, 1.18, 0.28]
$4 < z \leq 10.5$ (Pacucci & Loeb 2024)	Section 5.1.3, GW (eg1)	[-2.53, 1.02, 0.69]
	Section 5.1.3, GW (eg2)	[-3.04, 0.96, 0.69]
	Sections 5.2, 5.4	[-1.93, 1.05, 0.69]

APPENDIX B: GALAXY MERGER RATE ESTIMATED ASSUMING LOCAL SCALING RELATIONSHIP

In the appendix, we present the posterior distributions of model parameters in the Case 1 and Case 2 models in Fig. B1, and the reconstructed galaxy merger rate per galaxy from those posteriors in Fig. B2, by using the local $M_{\bullet} - M_{*}$ relationship (Kormendy & Ho 2013) and the GW datasets discussed in Section 5.1.3.

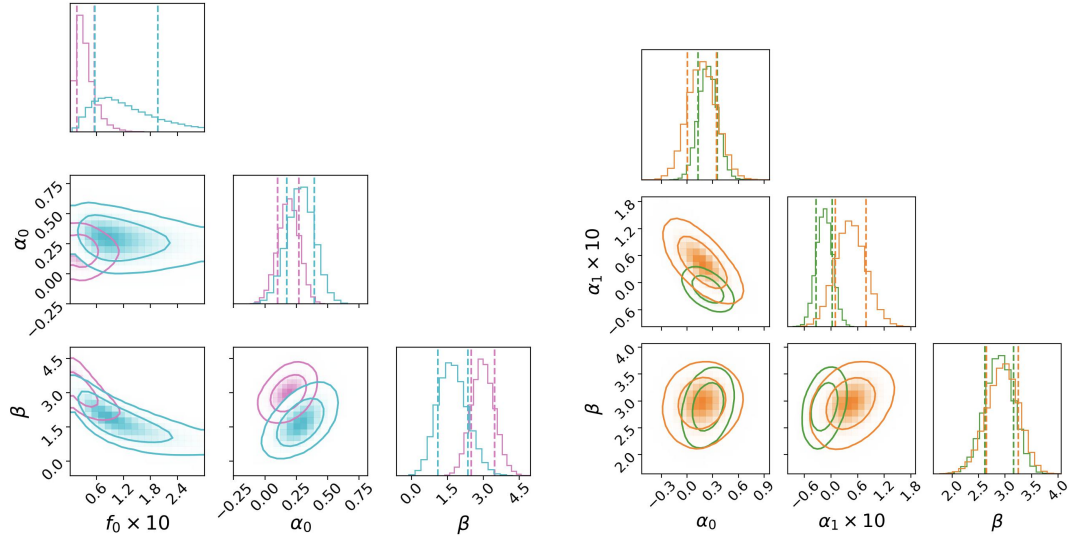


Figure B1. Left: posteriors of the model parameters in Case 1 model ($dN/dt =$) estimated from the first (pink) and second (cyan) realization of mock LISA data shown in Fig. 2, together with PTA detections of SGWB strain (Fig. 1). Right: posteriors of the model parameters in Case 2 model ($dN/dt =$) estimated from the first (green) and second (orange) realization of mock LISA data shown in Fig. 2, together with PTA detections of SGWB strain (Fig. 1).

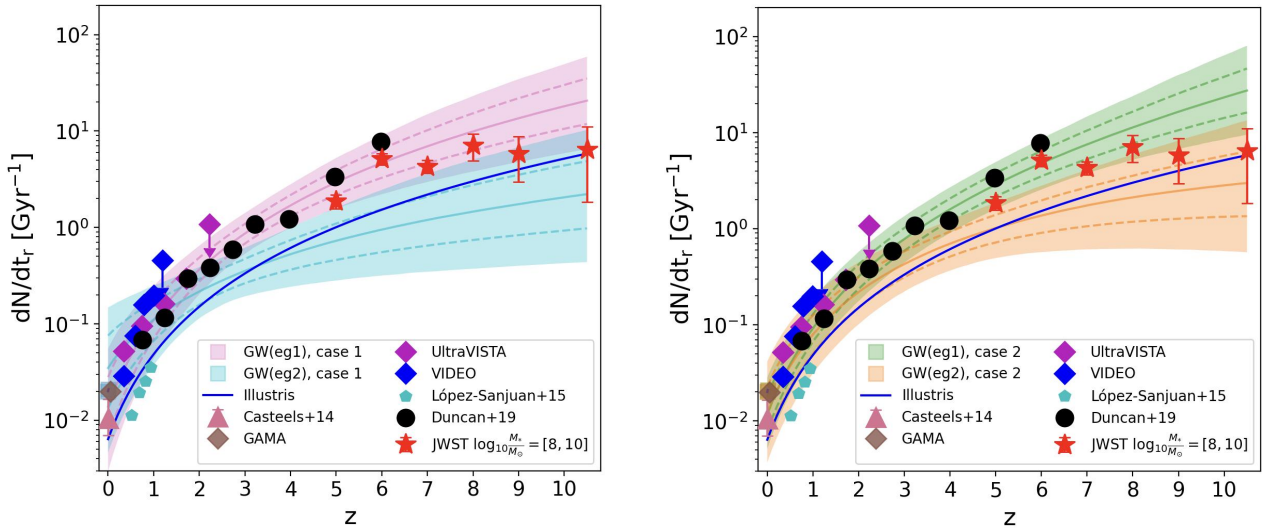


Figure B2. Similar to Fig. 5 but for Galaxy merger rate $\frac{dN}{dt_r}(z)$ estimated assuming local $M_\bullet - M_*$ relationship (Kormendy & Ho 2013) across the redshifts. The line styles in the left and right hand panels are the same to Fig. 5. The one sigma (bounded by dashed lines) and two sigma (shaded region) confidence region is plotted according to the posteriors results shown in Fig. B1.